This is the accepted version of the publication Yang, J., Su, Y., Liao, Y., Zhou, P., Xu, L., & Su, Z. (2022). Ultrasound tomography for health monitoring of carbon fibre–reinforced polymers using implanted nanocomposite sensor networks and enhanced reconstruction algorithm for the probabilistic inspection of damage imaging. Structural Health Monitoring, 21(3), 1110-1122 Copyright © The Author(s) 2021. DOI: 10.1177/14759217211023930.

Ultrasound Tomography for Health Monitoring of CFRPs Using Implanted Nanocomposite Sensor Networks and Enhanced RAPID Imaging

Jianwei Yang[a], Yiyin Su[a], Yaozhong Liao[a], Pengyu Zhou[a], Lei Xu[a],
and Zhongqing Su[a,b,c*]

[a] Department of Mechanical Engineering,
The Hong Kong Polytechnic University, Kowloon, Hong Kong SAR

[b] The Hong Kong Polytechnic University Shenzhen Research Institute
Shenzhen 518057, P.R. China

[c] School of Astronautics, Northwestern Polytechnical University, Xi'an, 710072, P.R. China

submitted to ***Structural Health Monitoring: An International Journal***

(submitted on 28 January 2021; revised and resubmitted on 6 May 2021)

---

[*] To whom correspondence should be addressed. Tel.: +852-2766-7818, Fax: +852-2365-4703,
Email: zhongqing.su@polyu.edu.hk (Prof. Zhongqing Su, *Ph.D.*)

Abstract

Irrespective of the popularity and demonstrated effectiveness of ultrasound tomography (UT) for damage evaluation, reconstruction of a precise tomographic image can only be guaranteed when a dense transducer network is used. However, a network using transducers such as piezoelectric wafers integrated with the structure under inspection unavoidably lowers local material strength and consequently degrades structural integrity. With this motivation, an implantable, nanocomposite-inspired, piezoresistive sensor network is developed for implementing *in-situ* UT-based structure health monitoring (SHM) of carbon fibre-reinforced polymer (CFRP) laminates. Individual sensors in the network are formulated with graphene nanosheets (GNSs) and polyvinylpyrrolidone (PVP), fabricated using a spray deposition process, and circuited via highly conductive carbon nanotube fibres (CNT-fibres) as wires, to form a dense sensor network. Sensors faithfully respond to ultrasound signals of megahertz. With ignorable intrusion to the host composites, the implanted sensor network, in conjunction with a UT approach that is enhanced by a revamped *reconstruction algorithm for the probabilistic inspection of damage* (RAPID)-based imaging algorithm, has proven capability of accurately imaging anomaly in CFRP laminates and continuously monitoring structural health status, while not at the cost of sacrificing the composites' original integrity.

***Keywords*:** CRFPs; structural health monitoring; ultrasound tomography; nanocomposite sensor

1. Introduction

Ultrasound tomography (UT), by virtue of its high accuracy, intuitive presentation of results and standardized implementation, has gained prominence in structural health monitoring (SHM)-driven integrity assurance and health management of engineering assets. With an analogous principle as the computed tomography (CT) using X-ray radiography in clinic, UT for SHM canvasses subtle variation in ultrasound signals by benchmarking pristine counterparts, subsequently associates the variation to material deterioration or damage occurrence, and projects evaluation results in pixelized images through proper tomographic imaging algorithms. UT for SHM has been the core of intensive research over the years. Representatively, Hinders *et al*. [1-5] are among those trailblazers who first exploited guided wave-based tomography. In this series of pioneering studies, comprehensive theory of implementing UT for damage detection was developed, with proven effectiveness in detecting flaws and anomalies in metallic and composite structures [3]. Jansen *et al*. [6] used Lamb waves to reconstruct tomographic images for visualizing defects in metallic and composite structures via an ultrasonic immersion. McKeon *et al*. [2, 3] compared the fan beam projection (FBP) and algebraic reconstruction technique (ART) – two popular approaches to implement UT, for characterizing damage in multi-layered aircraft structures, and concluded that ART showed higher accuracy and fidelity over FBP. Rose *et al*. [7, 8] extended the *reconstruction algorithm for probabilistic inspection of damage* (RAPID)-based tomographic imaging to damage localization and growth monitoring, and compared RAPID against FBP and ART, in terms of the image quality and image construction efficiency, to argue that RAPID offered higher flexibility in sensor network configuration, greater tolerance to ambient noise, and faster image construction with higher resolution.

Rao *et al*. [9, 10] proposed a full waveform inversion (FWI)-based tomography method and demonstrated its precision by evaluating the remaining wall thickness of an isotropic plate.

Nevertheless, regardless of the popularity and proven effectiveness of UT for SHM, implementation of UT usually entails a deliberately designed transducer network in a dense configuration, using commercially available transducers, as typified by metal-foil strain gauges [11], lead zirconate titanate (PZT) wafers [12-18], optical fibres [19], electromagnetic acoustic transducers (EMAT) [20], and piezoelectric polymer film-type sensors (*e.g.*, polyvinylidene fluoride (PVDF)) [21-26]. Among them, the sensitivity of strain gauges and piezoelectric polymer film-type sensors is limited inherently to signals of low frequencies (usually lower than hundred kilohertz [27]), as a result of the low piezoelectric coefficients that PVDF-type sensors possess [28]; PZT wafers are rigid and unwieldy to adapting to a curved surface, and a transducer network with multitudinous PZT wafers introduces intrusion to host structures; optical fibre-based sensors are fragile, necessitating extra protection, and in generally they are insensitive to damage far from sensor vicinity. Embedding optical fibres into a structure not only complicates the fabrication process but may degrade local material strength; EMATs are typically used for evaluation of metallic structures only, and moreover the transduction efficiency is normally insufficient compared with most piezoelectric transducers.

With an appropriately selected type of transducer, a transducer network can be either externally mounted on or internally embedded in composites to implement UT. However, a densely configured transducer network, when embedded, alters the microstructure of the fibre-reinforced matrix, influences the interlaminar stress distribution in the sensor vicinity, introduces artificial defect, and consequently lowers the structural load-carrying capacity, regardless of the fact that the intended role of the embedded transducer network is to monitor structural integrity degradation. On the other hand, any attempt to minimize such intrusion by limiting the transducer number is usually at the cost of undermining the detection resolution and accuracy, because reconstruction of a precise tomographic image is guaranteed by rich information that can only be provided by a dense transducer network. Indeed, it is a challenging task to strike a balance between the sensing cost (*i.e.*, the number of sensors) and sensing effectiveness (*i.e.*, the accuracy of tomography) when implementing UT-based SHM for composites using embedded transducers.

Recent advances in emerging nanotechnology have paved a new trail towards innovative sensors made of nanocomposites, to remarkably downsize a sensor but enhance its sensing capability. Nanocomposite sensors made of various carbon nanofillers (*e.g.*, carbon black, multi-walled carbon nanotubes, and graphene nanosheets) show appealing features such as low density, good flexibility, environmental and chemical stability, along with superb sensitivity. This category of sensors has secured the superiority in measurement, detection and monitoring. Favourable examples include the measurement of material strain induced by quasi-static loads [29, 30] or under low-frequency dynamic loads [31, 32], and identification of structural damage [33, 34]. Representatively, Zeng *et al.* [35, 36] developed a carbon black/PVDF sensor that was able to respond to dynamic responses in a broadband frequency regime from static strain, through medium-frequency structural vibration, to high-frequency ultrasound. Liu *et al.* [27] attempted a new nanocomposite sensor, coatable on a structural surface, in lieu of conventional PZT wafers. This type of sensor showed high fidelity, ultrafast response, and great sensitivity to broadband acoustic-ultrasonic signals, and captured signals were comparable with those obtained using commercial sensors such as PZT wafers. Liao *et al.* [37, 38] investigated a nano-engineered thin film-type piezoresistive sensor, coatable or sprayable on a structural surface for *in-situ* acquisition of dynamic strain up to 1.4 MHz. Nevertheless, traditional metallic cables and wires, to network individual sensors for forming a sensor network, are still of necessity in these approaches. The use of printed circuits [39, 40] may, to some extent, reduce the weight and volume of cables and wires, but the surface-mounted printed circuits show high likelihood of detachment from the host structures under cyclic loads.

In recognition of the deficiency of existing UT approaches for composite structures, a new breed of nanocomposite, piezoresistive sensor is developed using a spray deposition process. Individual sensors, deposited on a pre-treated B-stage epoxy film, are networked via highly conductive carbon nanotube fibres as wires, to form a dense sensor network. Flexible, light, sensitive to broadband dynamic signals, the sensor network is implanted into carbon fibre-reinforced polymer (CFRP) laminates, to fulfil guided ultrasonic waves (GUWs)-based UT. In conjunction with the use of the sensor network, the *reconstruction algorithm for the probabilistic inspection of damage* (RAPID)-based imaging algorithm is enhanced to facilitate processing of rich signals rendered by the sensor network and improve imaging accuracy. Experiment is conducted to investigate possible intrusion to the host composites from the implanted sensor network, demonstrate fidelity of acquired GUW signals, and examine accuracy of the enhanced RAPID algorithm.

2. Implantable Piezoresistive Sensor Network for UT of CFRPs

In a nutshell, a new nanocomposite ink is formulated with graphene nanosheets (GNSs) as the nanofiller and polyvinylpyrrolidone (PVP) as the matrix, which is deposited on a pre-cured B-stage epoxy membrane using a spray deposition process, to fabricate individual sensing units. Thus-produced sensing units are circuited via highly conductive carbon nanotube fibres (CNT-fibres), to form a dense sensor network, which is implanted into CFRP laminates for conducting *in situ* UT-based SHM.

2.1. Pre-curing of B-staged Epoxy Film

For fabricating a compatible, implantable sensing unit with minimized intrusion to the host composites, a B-staged epoxy is pre-cured for depositing sensing units and unit-associated wires/circuits, and in the meantime insulating sensing units from conductive fibres in CFRPs. A high temperature-resistant release film (AIRTECH® WL5200B nonperforated peel ply) is selected as the substrate, onto which the B-staged epoxy is deposited. The release film is immersed in acetone and sonicated in an ultrasonic bath (Branson® 5800 Ultrasonic Cleaner, 40 kHz) for 30 min to remove contaminants, and is heated at 65 °C in a vacuum oven for 15 min to evaporate the residual acetone. The B-staged epoxy is poured on one end of the release film and then evenly squeezed to the other end of the film using an applicator at 80 °C. The thickness of the coated B-staged epoxy is ~20 μm, measured using an electronic spiral micrometre. Up to this stage, the B-staged epoxy on the film is still chemically reactive. To reduce the resin flowability and maintain a desired morphology of the spray-coated sensing units, the epoxy film is pre-cured in a vacuum environment at 130 °C to achieve 40 % of the full degree of curing.

2.2. Fabrication of Spray-coated Nanocomposite Sensing Units

A standard solution mixing process is applied to prepare nanocomposite ink. PVP (Sigma-Aldrich® PVP K-30) is chosen as the matrix, and GNSs (TANFENG®, thickness: ~1 nm, diameter: ~50 μm, SSA: ~1200 m^2/g, and purity: > 99 wt.%) as the modified nanofillers (mass ratio of GNSs to PVP is 1:19). The GNS/PVP hybrid (1 g) is dispersed in ethanol (20 ml), and magnetically stirred at 500 rpm at an ambient temperature (25 °C) for 2 h, followed with a sonication in the ultrasonic bath for 1 h. Thus-produced nanocomposite ink is sprayed directly onto the above prepared pre-cured epoxy film using an airbrush (HD-130). The scanning speed of the nozzle (5 cm/s), stream pressure (0.35 MPa) and distance of target to nozzle (10 cm) are precisely controlled during the spraying process, to warrant a consistent initial resistance of the ink. During deposition, the B-staged epoxy is adhesive, in which a small amount of ethanol remains, and the morphology of the ink tends to be affected by the residual ethanol in the subsequent procedure of heating treatment. To eliminate such effect, the ink deposited on the pre-cured epoxy film is placed in a frozen drying oven to vaporize the residual ethanol.

During the spraying process, a thin polyimide (PI) film with a desired hollowed-out is prepared, serving as a moulding layer. The film is pressed onto the pre-cured epoxy film. The hollowed-out precisely defines the geometry of a sensing unit, to be 5 mm in width and 20 mm in length, after the nanocomposite ink is sprayed on the PI film and then the moulding layer is peeled off from the pre-cured epoxy film. A pair of electrodes is introduced to each sensing unit, by aligning two CNT-fibres (DexMat® CNT-film) along the two long edges of a unit. Another identical pre-cured B-staged epoxy film is placed atop each sensing unit which has been deposited on the substrate, whereby to encapsulate each sensing unit and insulated it from conductive fibres upon implantation into CFRPs. Each encapsulated sensing unit is fully cured at 130 °C for 30 min under a vacuum condition. With such a manufacturing approach, the thickness of each sensing unit is ~45 μm only, measured in scanning electron microscope (SEM) images, inflicting minimal intrusion to the host composites. The manufacturing procedure of preparing the nanocomposite sensing units is flowcharted in **Fig. 1**, and thus-fabricated sensing units with CNT-fibre-based electrodes and wires are photographed in **Fig. 2**. With a resistance of ~20 Ω/m only, the CNT-fibres also function as wires to network individual sensing units. The wire is ~1 mm in width and ~10 μm in thickness only, impacting ignorable intrusion to the composites.

2.3. Implantation of Sensor Network into CFRP Laminates

A series of quasi-isotropic CFRP laminates (500 × 500 × 1.15 mm^3) is prepared in accordance with a standard autoclaving procedure. Each laminate is of 8-layer unidirectional prepregs (T300, Torayca®) with the stacking sequence of $[0°/90°/45°/-45°]_s$. For proof-of-concept validation, 16 sensing units are networked with CNT-fibre-based wires to form a sensor network, which is then implanted between the 4th and 5th layers of each laminate during autoclaving, as illustrated schematically in **Fig. 3**. The autoclave mould is heated at a rate of 1.5 °C /min from an ambient temperature to 80 °C, followed with a post-curing at 130 °C for another 1 h. The curing pressure remains at 160 psi. The strong adhesion of prepreg and high pressure of autoclaving ensure accurate position of each sensing unit in the CFRP laminate upon fabrication. Upon full curing, the nominal thickness of each laminate measures ~1.15 mm. Each laminate is trimmed using a water jet cutter (OMAX® PROTOMAX).

2.4. Morphological Characterization

Morphological characterization of the spray-coated sensing units is performed using scanning electron microscopy (SEM) (TESCAN® Vega 3), to observe good homogeneity, **Figs. 4(a)** and **(b)**, in which the GNS aggregates are observed to distribute in PVP densely and evenly. Such a trait is conducive to the creation of a uniform conductive network in the sensing unit. **Figures 4(c)** and **(d)** show the intersection of the CFRP laminate with an implanted sensing unit (cross-section view), to reveal that the interface between the CFRP laminate and implanted sensing unit is indistinguishable, implying an ignorable intrusion of the implanted sensor network to the host composites.

2.5. Mechanical Properties of CFRP Laminates with Implanted Sensor Network

Quasi-static tensile test, in accordance with ASTM D3039 [41], is performed to gauge possible degradation in tensile properties and change in failure modes of the CFRP laminates owing to the implantation of a sensor network. To this end, two types of CFRP laminates are fabricated with and without an implanted sensing unit, each measuring 250 × 25 × 1.15 mm^3. Both laminates are adhered with two aluminium end tabs before test to avoid premature failure around the gripping device (Scotch-Weld® 2216 Epoxy Adhesive). Laminates are pulled at a constant crosshead speed of 2 mm/min on a universal testing system (INSTRON® 5982) until the fracture, during which strain is recorded using an advanced video extensometer (AVE). **Figure 5** represents the tensile testing results of the two types of laminates, to note no measurable difference in between. The averaged tensile moduli of the two types of laminates are 45.86 GPa and 44.80 GPa, respectively, implying a slight decrease of ~2.31% only, due to the implantation of the sensing unit. The slight variation in failure tensile stress/strain between laminates with and without an implanted sensing unit is attributed to the discrepancy in specimen preparation and tests.

3. Enhanced RAPID Imaging

Conventional UT by virtue of imaging algorithms including FBP, ART, FWI and RAPID often shows inferior accuracy when insufficient sensors are used, due to the narrow scanning angle and inadequate number of sensing path available in the sensor network, during tomographic image reconstruction – a deficiency referred to as *limited-angle problem* [42]. The limited-angle scanning can make signal acquisition incomplete, potentially leading to ignorance of damage in certain areas within the inspection region. To warrant a broad scanning angle and sufficient sensing paths, sensors have to be configured in a dense manner. Using the developed implantable sensing units, in conjunction with the use of only a handful of surface-mounted PZT wafers as excitation sources, a dense transducer network can be configured, to circumvent the *limited-angle problem* that conventional UT-based imaging algorithms may have.

In addition, aimed at precisely estimating the geometrical features and severity of defect (e.g., uneven resin during curing, or impact-induced delamination), conventional RAPID algorithm is revamped here, in which the probability of a defect presence at a pixel within the inspection region is calibrated, in terms of (i) the severity of defect-induced change in signals captured by different sensing paths, and (ii) the relative position of the defect with regard to all sensing paths in the transducer network. To quantify defect-induced change in signals, signal difference coefficient (SDC) – a GUW feature, is defined for tomographic imaging. SDC is statistical difference in signals between the current status and the reference status, which reads

$$\mathrm{SDC} = 1 - (\mathrm{Cov}(X, Y) / \sigma_X \sigma_Y), \tag{1}$$

where Cov(X, Y) signifies the covariance of the reference signal X and the current signal Y, given by

$$\mathrm{Cov}(X, Y) = \sum_{k=1}^{K} (X_k - \mu_X)(Y_k - \mu_Y), \tag{2}$$

and

$$\sigma_X \sigma_Y = \sqrt{\sum_{k=1}^{K} (X_k - \mu_X)^2} \sqrt{\sum_{k=1}^{K} (Y_k - \mu_Y)^2}, \tag{3}$$

where X_k and Y_k (k=1, 2, …, K) are discretized forms of X and Y, each with K discretized data; μ_X and μ_Y are the mathematical expectation of X and Y. The defect distribution probability, $P(x, y)$, can be defined as a linear summation of SDC calculated by all sensing paths rendered by the transducer network with a total of M transmitters and N receivers, as

$$P(x, y) = \sum_{i=1}^{M} \sum_{j=1}^{N} P_{ij}(x, y) = \sum_{i=1}^{M} \sum_{j=1}^{N} \mathrm{SDC}_{ij} w_{ij}(x, y), \tag{4}$$

where (x, y) is the coordinate of an arbitrary point within the inspection region; $P_{ij}(x, y)$ denotes the probability of defect occurrence at (x, y) that is estimated by the sensing path linked by transmitter i (located at (x_i, y_i)) and receiver j (located at (x_j, y_j)); SDC_{ij} is the SDC value calculated by that sensing path; $w_{ij}(x, y)$ signifies the weighted matrix related to the spatial distribution of the defect, and it, for the sensing path i-j, is defined as

$$w_{ij}(x, y) = (\beta - R_{ij}(x, y)) / (\beta - 1), \tag{5}$$

and

$$R_{ij}(x, y) = (l_{(x,y)\to(x_i,y_i)} + l_{(x,y)\to(x_j,y_j)}) / l_{(x_i,y_i)\to(x_j,y_j)}, \tag{6}$$

where l is the distance between the two points indicated in subscript; β is a scaling parameter which controls the size of the effective elliptical distribution area, and the amplitude of which tapers from its maximum value along the line connecting the two ellipse foci to zero on the periphery of the ellipse [43], as illustrated in **Fig. 6**.

Provided that an unreasonably small value of β is selected, artifacts can be introduced in the reconstructed image; in the contrast, imaging resolution degrades if β is unjustly large. In prevailing RAPID algorithms, the scaling parameter β is usually selected as the consistent of 1.05, with the assumption that the distances from the defect to all the sensing units are the same – that, however, is not the case in reality. It is therefore that the selection of a constant parameter β is inadequate to warrant accurate depiction of defect when the defect is at an arbitrary position within the inspection region.

In this enhanced RAPID imaging algorithm, based on the principle of iteration, the scaling parameter β and the defect distribution probability $P(x, y)$ is continuously iterated and updated, using every single sensing path in the transducer network, after initial calculation of the approximate defect location using Eqs. (1) – (6), as

$$\beta^{n+1} = R_{ij}(x_d^n, y_d^n) = (l_{(x_i,y_i)\rightarrow(x_d^n,y_d^n)} + l_{(x_j,y_j)\rightarrow(x_d^n,y_d^n)}) / l_{(x_i,y_i)\rightarrow(x_j,y_j)}, \tag{7}$$

and

$$P^{n+1}(x,y) = \sum_{i=1}^{M}\sum_{j=1}^{N} P_{ij}^{n+1}(x,y) = \sum_{i=1}^{M}\sum_{j=1}^{N} \mathrm{SDC}_{ij} w_{ij}^{n}(x,y), \tag{8}$$

where (x_d^0, y_d^0) is the coordinate of the defect as initially estimated by Eqs. (1) – (6), and (x_d^n, y_d^n) the coordinate of the updated location after n iterations. In each iteration, β and $P_{ij}(x, y)$ for a sensing path is updated in accordance with the defect location determined by previous paths. It can be derived from Eq. (8) that if the distance of the defect to all sensing paths is identical, the values of the scaling parameter β are a constant; otherwise the values can be various based on the distances. Continuous updating β and $P(x, y)$ not only improves the accuracy of defect localization, but also enhances the geometrical depiction and severity estimate of the defect.

4. Experimental Validation: UT-based Anomaly Imaging Using Implanted Sensor Network and Enhanced RAPID

4.1. Acquisition of GUWs Using Implanted Sensor Network

To experimentally examine the fidelity of the spray-coated sensing units for perceiving GUW signals in a broadband frequency regime, two CFRP laminates are prepared, with the identical configuration as that of the laminates detailed in Section 2.3. Four PZT wafers (labelled as P1 – P4) (PSN-33, Ø 12 mm, 1 mm thick) – used as wave actuators – are surface-mounted on each CFRP laminate, see **Fig. 7**. One of the two CFRP laminates is pre-implanted with a sensor network comprising 16 nanocomposite sensing units (denoted by S1 – S16) between the 4th and 5th layers which are arranged in circular fashion – used as the wave receivers; and the other laminate is pre-embedded with a PZT wafer (PSN-33, Ø 12 mm, 1 mm thick) between the 4th and 5th layers as a benchmark laminate, for comparison and calibration.

The experimental set-up is shown in **Fig. 8**. In the set-up, the signal generation module consists of an arbitrary waveform generator on NI® PXIe-1071 platform, and a linear power amplifier (Ciprian® US-TXP-3); the data acquisition module includes a self-developed amplification unit for mitigating ambient noise, a resistor-adjustable

Wheatstone bridge converting piezoresistive variation to electrical signals, and an oscilloscope (Agilent® DSO 9064A). Four PZT wafers are connected with the signal generation module, while the implanted sensor network and the embedded PZT wafer are respectively linked to the data acquisition module.

A series of five-cycle Hanning-function-modulated sinusoidal tonebursts with the central frequency varying from 150 kHz to 450 kHz (with an increment of 25 kHz) is generated with the arbitrary waveform generator, and applied on each PZT wafer in turn via the power amplifier, to emit GUWs into CFRP laminates. The modulated excitation provides concentrated energy in a narrowed frequency band, efficiently reducing wave dispersion and benefiting signal interpretation. **Figure 9** compares the signals, generated by P1 at 175 kHz, captured by S5 (i.e., the sensing path P1 − S5), against the counterpart signal captured by the embedded PZT wafer in the benchmark laminate. Captured signals are processed with a first-order Butterworth filter to eliminate measurement noise. The first-arriving wave component (i.e., the zeroth-order symmetric Lamb wave mode, denoted by S_0 in what follows) is clearly observed in both signals, showing quantitative agreement in terms of the arrival time and signal waveform. Not only the S_0 mode but also the zeroth-order anti-symmetric Lamb wave mode (denoted by A_0) is faithfully captured by the sensing units. **Figure 10** comparatively presents the signals captured by the same sensing path (P1 − S5) at 150, 175, 200, 225, and 250 kHz, respectively, arguing that the magnitudes of both the S_0 and A_0 modes are dependent on the excitation frequency. The maximum magnitudes of both wave modes are recorded at 175 kHz, as at this frequency the PZT wave actuator resonates. Sweeping the excitation frequency from 150 to 450 kHz, **Fig. 11** shows the spectrum of signals captured via P1 − S5, compared with the counterpart spectrum obtained by the embedded PZT wafer, to observe no remarkable discrepancy in sensing performance between these two types of sensor over a broad frequency range.

To further examine the sensitivity of the nanocomposite sensing unit when it is internally embedded in or surface-mounted on CFRP composites, an additional sensing unit is mounted atop the benchmark laminate. **Figure 12** displays the signals captured by the implanted and surface-mounted sensing units, respectively, showing good accordance in between. Note that the crosstalk included in signals at the commencement of excitation is generated by the high-voltage power amplifier, which, however, does not interfere with signal interpretation.

4.2. Proof-of-Concept: Anomaly Imaging

A steel cylinder (diameter: 20 mm, mass: 200 g) is surface-coupled with the above CFRP with the implanted sensor network using glycerol as a coupling agent, as artificial anomaly. Note the CFRP laminate before introduction of the artificial anomaly is used as the reference condition for imaging. In view of the transducer network configuration (four PZT wafers as actuators and 16 nanocomposite sensing units as receivers, in **Fig. 8**), a total of 60 sensing paths are technically available. As a typical signal for illustration, **Fig. 13** compares the signals generated by P1 at 175 kHz and captured by S5, before and after the anomaly is introduced. Using Eq. (1), SDC values for all the sensing paths are calculated and presented in **Fig. 14**. The SDC value for the sensing path P1 – S5, which reads 0.0328, is higher than those for other sensing paths in which P1 serves as the actuator, **Fig. 14(a)**, implying higher possibility of defect presence along P1 – S5.

Similarly, higher SDC values are also observed for P2 – S1, P3 – S3 and P4 – S3, in **Fig. 14(b)**, **(c)** and **(d)**, respectively. With calculated SDC values throughout the entire transducer network, the tomographic images are constructed using the conventional and enhanced RAPID algorithms (Eqs. (4) – (8)), respectively, in **Fig. 15**. It is apparent that there is no remarkable difference in the accuracy of anomaly positioning for two algorithms, while the enhanced RAPID algorithm using the iteratively updated scaling parameter β based on Eq. (7) shows superior accuracy when evaluating the shape of the anomaly, compared with the conventional algorithm which forces β as a constant of 1.05.

5. Conclusions

In the present study, a new breed of implanted nanocomposite sensor network is developed, for implementing *in-situ*, UT-driven SHM of CFRPs. Individual sensing units are formulated with GNSs/PVP using a spray deposition process, circuited with highly conductive CNT-fibres as wires, and then implanted into CFRP laminates to form a dense sensor network. The implanted sensor network inflicts ignorable degradation of the composite's original integrity. The use of CNT-fibres as wires for networking sensing units significantly reduces the weight and volume added to original composites. Results have proven the capability of the developed sensing units in perceiving GUWs in a broad frequency regime with high precision up to 450 kHz. The enhanced RAPID algorithm presents superior accuracy, compared with the conventional RAPID algorithm, when used to evaluate both the location and shape of anomaly, endowing the UT-based SHM with higher imaging resolution.

Acknowledgements

The work was supported by a General Project (No. 51875492) and a Key Project (No. 51635008) received from the National Natural Science Foundation of China. Z Su acknowledges the support from the Hong Kong Research Grants Council via General Research Funds (Nos. 15202820, 15204419 and 15212417).

References

[1] Hinders, Mark K., *et al*. "Contact scanning Lamb wave tomography." The Journal of the Acoustical Society of America 104.3 (1998): 1790-1791.

[2] McKeon, James C., *et al*. "Parallel projection and crosshole Lamb wave contact scanning tomography." The Journal of the Acoustical Society of America 106.5 (1999): 2568-2577.

[3] Malyarenko, Eugene V., *et al*. "Fan beam and double crosshole Lamb wave tomography for mapping flaws in aging aircraft structures." The Journal of the Acoustical Society of America 108.4 (2000): 1631-1639.

[4] Leonard, Kevin R., *et al*. "Ultrasonic Lamb wave tomography." Inverse Problems 18.6 (2002): 1795.

[5] Leonard, Kevin R., *et al*. "Multi-mode Lamb wave tomography with arrival time sorting. " The Journal of the Acoustical Society of America 117.4 (2005): 2028-2038.

[6] Jansen, D. P., *et al*. "Lamb wave tomography of advanced composite laminates containing damage." Ultrasonics 32.2 (1994): 83-90.

[7] Hay, T. R., *et al*. "A comparison of embedded sensor Lamb wave ultrasonic tomography approaches for material loss detection." Smart Materials and Structures

15.4 (2006): 946.

[8] Yan, Fei, *et al*. "Ultrasonic guided wave imaging techniques in structural health monitoring." Journal of intelligent material Systems and Structures 21.3 (2010): 377-384.

[9] Rao, Jing, *et al*. "Guided wave tomography based on full waveform inversion." IEEE Transactions on Ultrasonics, Ferroelectrics, and Frequency Control 63.5 (2016): 737-745.

[10] Rao, Jing, *et al*. "Investigation of the reconstruction accuracy of guided wave tomography using full waveform inversion." Journal of Sound and Vibration 400 (2017): 317-328.

[11] Boukellif, Ramdane, *et al*. "Parameter identification of crack-like notches in aluminum plates based on strain gauge data." Structural Health Monitoring (2020): 1475921720981845.

[12] Yadav, Susheel Kumar, *et al*. "Reliability of crack quantification via acousto-ultrasound active-sensing structural health monitoring using surface-mounted PZT actuators/sensors." Structural Health Monitoring (2020): 1475921720921536.

[13] Si, Liang, *et al*. "Online structural state assessment for aerospace composite structures using an acousto-ultrasonics-based multi-damage index identification approach." Structural Health Monitoring (2020): 1475921719899334.

[14] Sikdar, Shirsendu, *et al*. "Nonlinear elastic wave propagation and breathing-debond identification in a smart composite structure." Composites Part B: Engineering 200 (2020): 108304.

[15] Su, Zhongqing, *et al*. "A built-in active sensor network for health monitoring of composite structures." Smart Materials and Structures 15.6 (2006): 1939.

[16] Qing, Xinlin P., *et al*. "Advances in the development of built-in diagnostic system for filament wound composite structures." Composites Science and Technology 66.11-12 (2006): 1694-1702.

[17] Masmoudi, Sahir, *et al*. "Use of piezoelectric as acoustic emission sensor for *in-situ* monitoring of composite structures." Composites Part B: Engineering 80 (2015): 307-320.

[18] Dziendzikowski, Michal, *et al*. "*In-situ* barely visible impact damage detection and localization for composite structures using surface mounted and embedded PZT transducers: A comparative study." Mechanical Systems and Signal Processing 78 (2016): 91-106.

[19] Loutas, T. H., *et al*. "Reliability of strain monitoring of composite structures via the use of optical fiber ribbon tapes for structural health monitoring purposes." Composite Structures 134 (2015): 762-771.

[20] Mei, Hanfei, *et al*. "Pure S0 and SH0 detections of various damage types in aerospace composites." Composites Part B: Engineering (2020): 107906.

[21] Saber, Nasser, *et al*. "Smart thin-film piezoelectric composite sensors based on high lead zirconate titanate content." Structural Health Monitoring 14.3 (2015): 214-227.

[22] Burton, Andrew R., *et al*. "Bio-compatible wireless inductive thin-film strain sensor for monitoring the growth and strain response of bone in osseointegrated prostheses." Structural Health Monitoring (2019): 1475921719831452.

[23] Giri, Paritosh, *et al*. "Characterization of carbon fiber reinforced polymer strengthened concrete and gap detection with a piezoelectric-based sensory technique." Structural Health Monitoring 18.1 (2019): 172-179.

[24] Ghafari, Ehsan, *et al*. "Self-polarized electrospun polyvinylidene fluoride (PVDF)

nanofiber for sensing applications." Composites Part B: Engineering 160 (2019): 1-9.

[25] Jung, Kyung-Chae, *et al*. "Performance evaluation of smart grid fabrics comprising carbon dry fabrics and PVDF ribbon sensors for structural health monitoring." Composites Part B: Engineering 163 (2019): 690-701.

[26] Choi, Kyungwho, *et al*. "Impact monitoring characteristics of piezoelectric paint sensor by thermal fatigue analysis for railroad vehicle applications." Structural Health Monitoring 19.6 (2020): 1951-1962.

[27] Liu, Menglong, *et al*. "Applications of a nanocomposite-inspired *in-situ* broadband ultrasonic sensor to acousto-ultrasonics-based passive and active structural health monitoring." Ultrasonics 78 (2017): 166-174.

[28] Payo, Ismael, *et al*. "Dynamic characterization of piezoelectric paint sensors under biaxial strain." Sensors and Actuators A: Physical 163.1 (2010): 150-158.

[29] Hu, Ning, *et al*. "Investigation on sensitivity of a polymer/carbon nanotube composite strain sensor." Carbon 48.3 (2010): 680-687.

[30] Li, Weikang, *et al*. "Carbon nanotube-graphene nanoplatelet hybrids as high-performance multifunctional reinforcements in epoxy composites." Composites Science and Technology 74 (2013): 221-227.

[31] Qiu, Ling, *et al*. "Ultrafast dynamic piezoresistive response of graphene-based cellular elastomers." Advanced Materials 28.1 (2016): 194-200.

[32] Zhou, Pengyu, *et al*. "An inkjet-printed, flexible, ultra-broadband nanocomposite film sensor for *in-situ* acquisition of high-frequency dynamic strains." Composites Part A: Applied Science and Manufacturing 125 (2019): 105554.

[33] Sebastian, James, *et al*. "Health monitoring of structural composites with embedded

carbon nanotube coated glass fiber sensors." Carbon 66 (2014): 191-200.

[34] Cao, Wuxiong, *et al*. "A Spray-on, Nanocomposite-based sensor network for *in-situ* active structural health monitoring." Sensors 19.9 (2019): 2077.

[35] Zeng, Zhihui, *et al*. "A coatable, light-weight, fast-response nanocomposite sensor for the *in-situ* acquisition of dynamic elastic disturbance: From structural vibration to ultrasonic waves." Smart Materials and Structures 25.6 (2016): 065005.

[36] Zeng, Zhihui, *et al*. "Ultra-broadband frequency responsive sensor based on lightweight and flexible carbon nanostructured polymeric nanocomposites." Carbon 121 (2017): 490-501.

[37] Liao, Yaozhong, *et al*. "Ultrafast response of spray-on nanocomposite piezoresistive sensors to broadband ultrasound." Carbon 143 (2019): 743-751.

[38] Liao, Yaozhong, *et al*. "An ultra-thin printable nanocomposite sensor network for structural health monitoring." Structural Health Monitoring (2019): 1475921719859338.

[39] Qiu, Lei, *et al*. "Impact monitoring for aircraft smart composite skins based on a lightweight sensor network and characteristic digital sequences." Sensors 18.7 (2018): 2218.

[40] Wang, Yu, *et al*. "A stretchable and large-scale guided wave sensor network for aircraft smart skin of structural health monitoring." Structural Health Monitoring (2019): 1475921719850641.

[41] ASTM Committee D-30 on Composite Materials. Standard test method for tensile properties of polymer matrix composite materials. ASTM International, 2008.

[42] Hubmer, Simon, *et al*. "Limited-angle acousto-electrical tomography." Inverse Problems in Science and Engineering 27.9 (2019): 1298-1317.

[43] Sheen, Bongjae, *et al*. "A study on quantitative lamb wave tomogram via modified RAPID algorithm with shape factor optimization." International Journal of Precision Engineering and Manufacturing 13.5 (2012): 671-677.

Figures

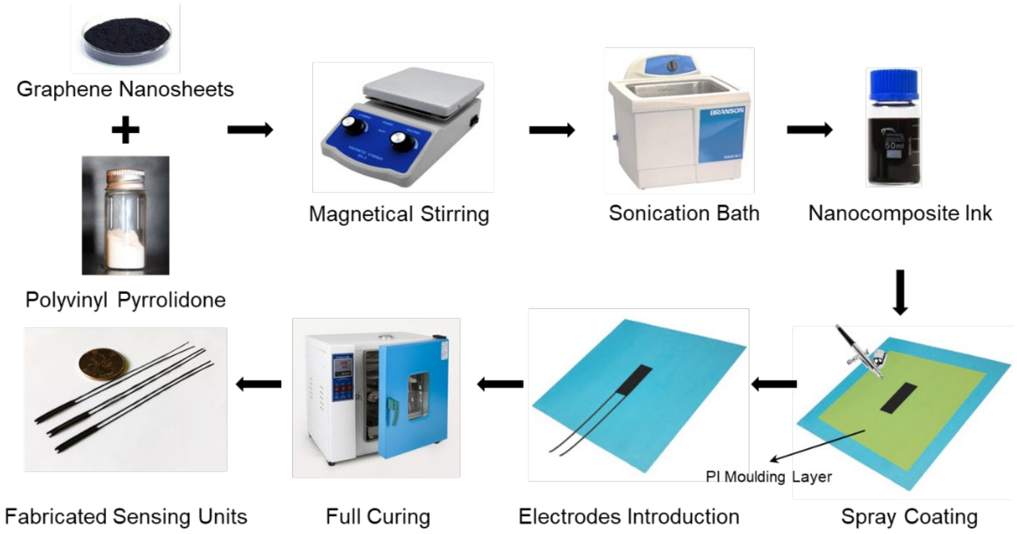

Fig. 1. Flowchart of fabricating the spray-coated nanocomposite sensing units.

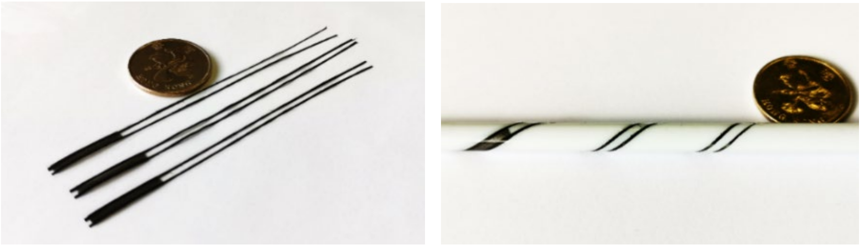

(a) **(b)**

Fig. 2. Photographs of (a) fabricated nanocomposite sensing units; (b) sensing unit showing a high degree of flexibility (diameter of the plastic rod in photo: 8 mm)

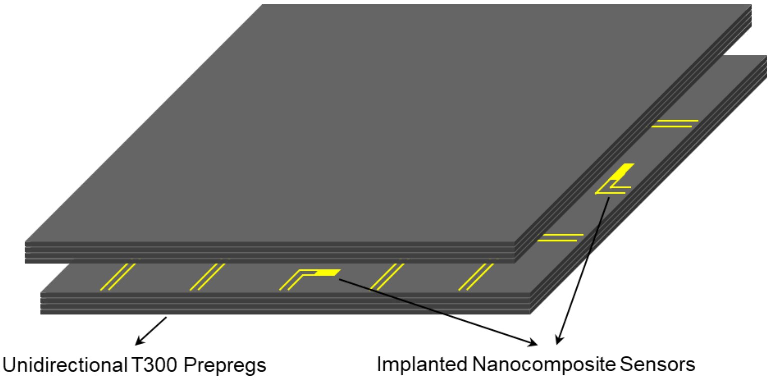

Fig. 3. Schematic illustration of a CFRP laminate with an implanted sensor network comprising nanocomposite sensing units.

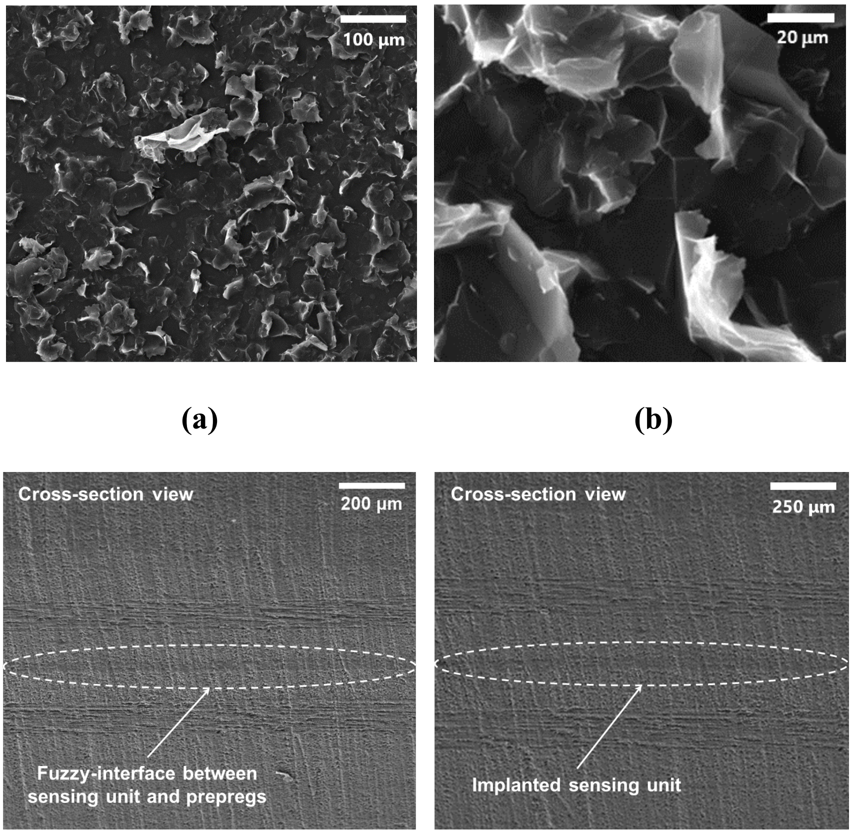

(a) **(b)**

(c) **(d)**

Fig. 4. SEM images of (a, b) spray-coated nanocomposites showing densely and evenly distributed GNSs in PVP, in two different scales; (c, d) intersecting surface of CFRP laminate with an implanted sensing unit showing ignorable intrusion of the sensing unit to the host composites.

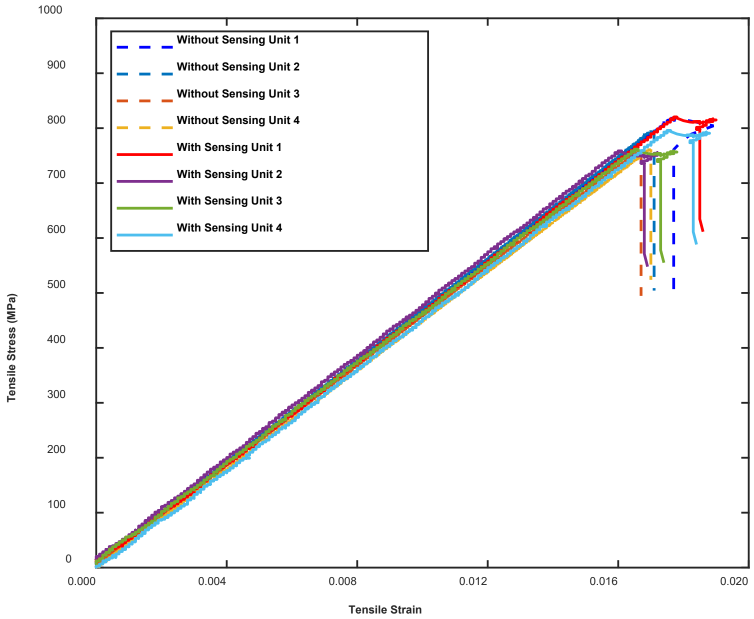

Fig. 5. Tensile strain-stress relation of CFRP laminates with and without an implanted sensing unit.

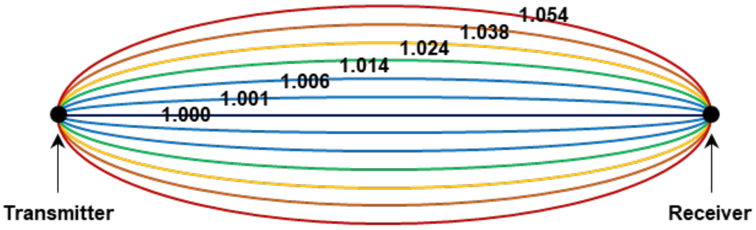

Fig. 6. Illustration of the elliptical distribution area of the RAPID algorithm.

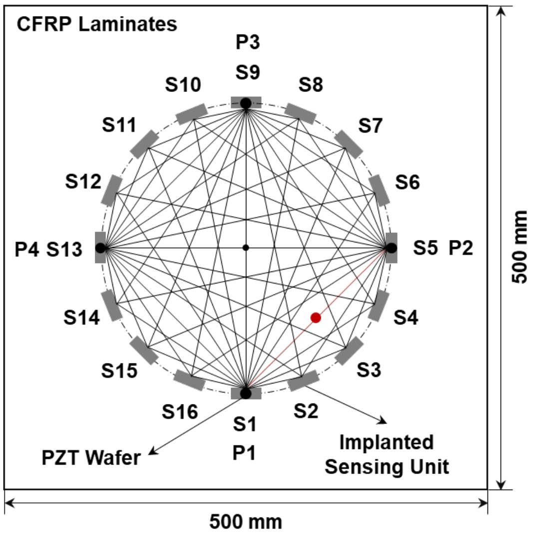

Fig. 7. Dimensional sketch of the CFRP laminate with an implanted sensor network. (black dot: PZT wafer as wave actuator; grey rectangular: implanted sensing unit)

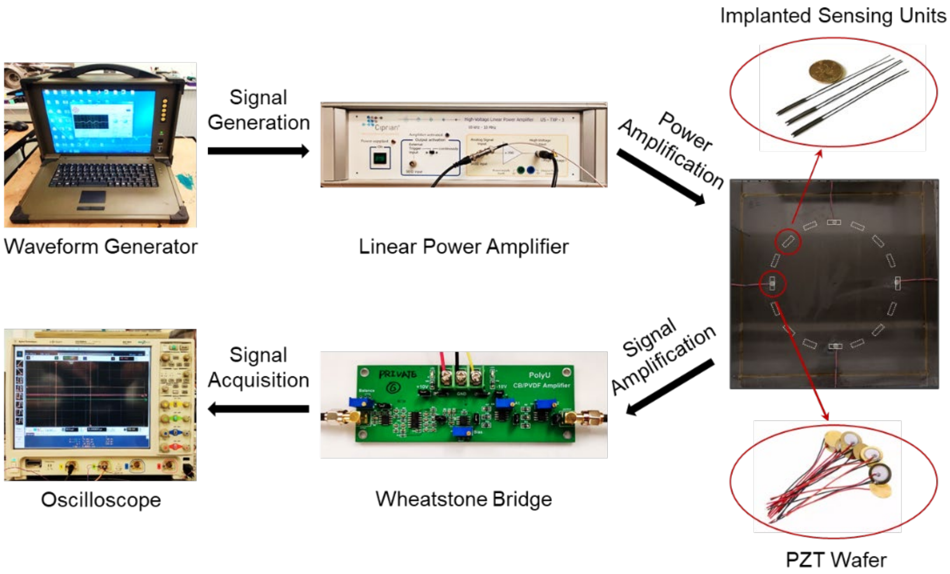

Fig. 8. Experimental set-up for *in-situ* acquisition of GUWs using nanocomposite sensing units.

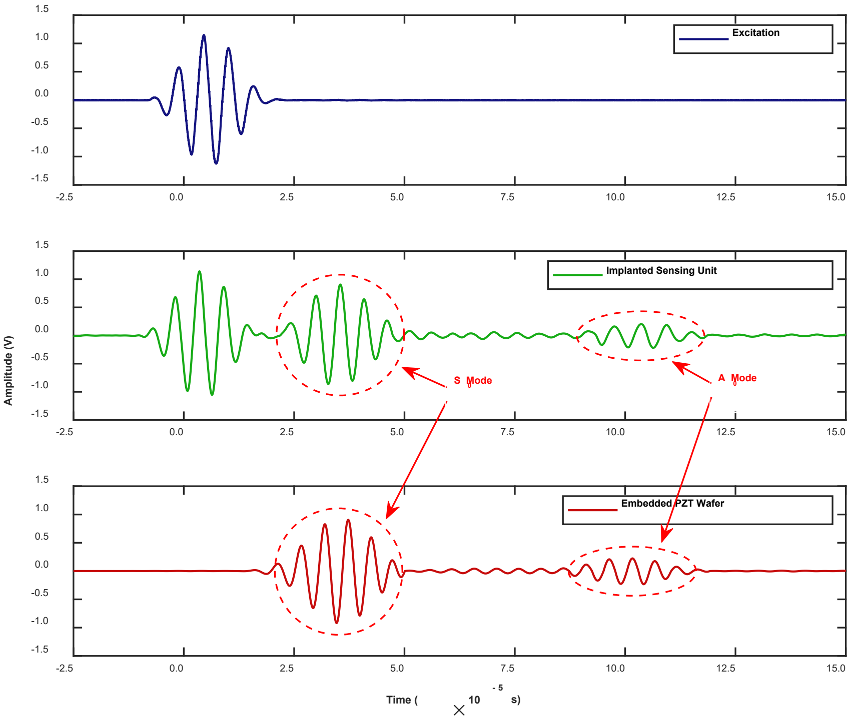

Fig. 9. GUWs signals respectively captured by the implanted sensing unit and embedded PZT wafer along sensing path P1 – S5 at 175 kHz.

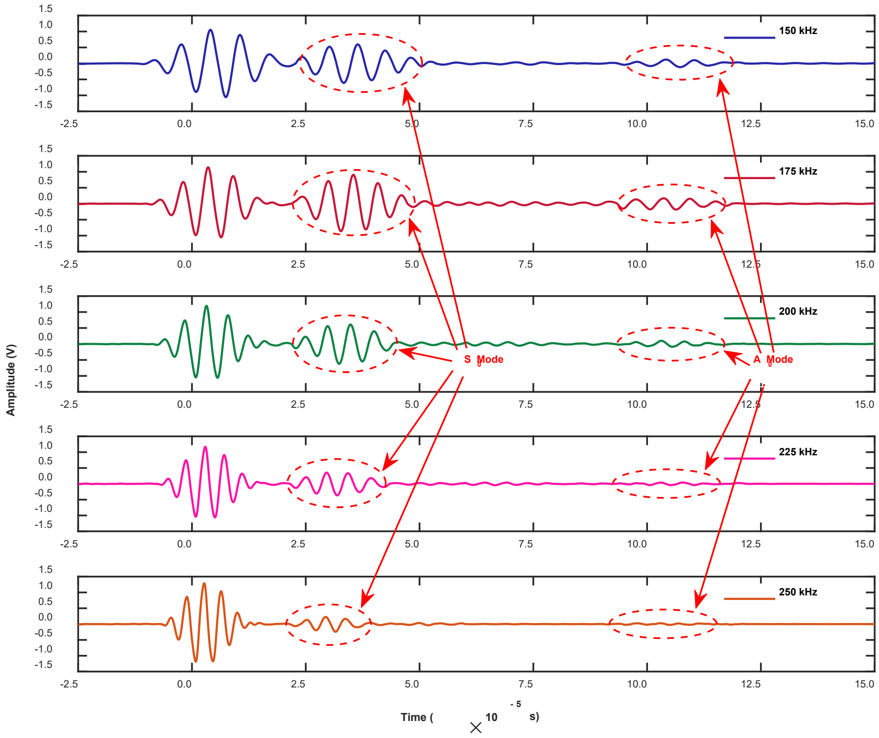

Fig. 10. GUWs signals respectively captured by the implanted sensing unit along sensing path P1 – S5 at 150, 175, 200, 225, and 250 kHz.

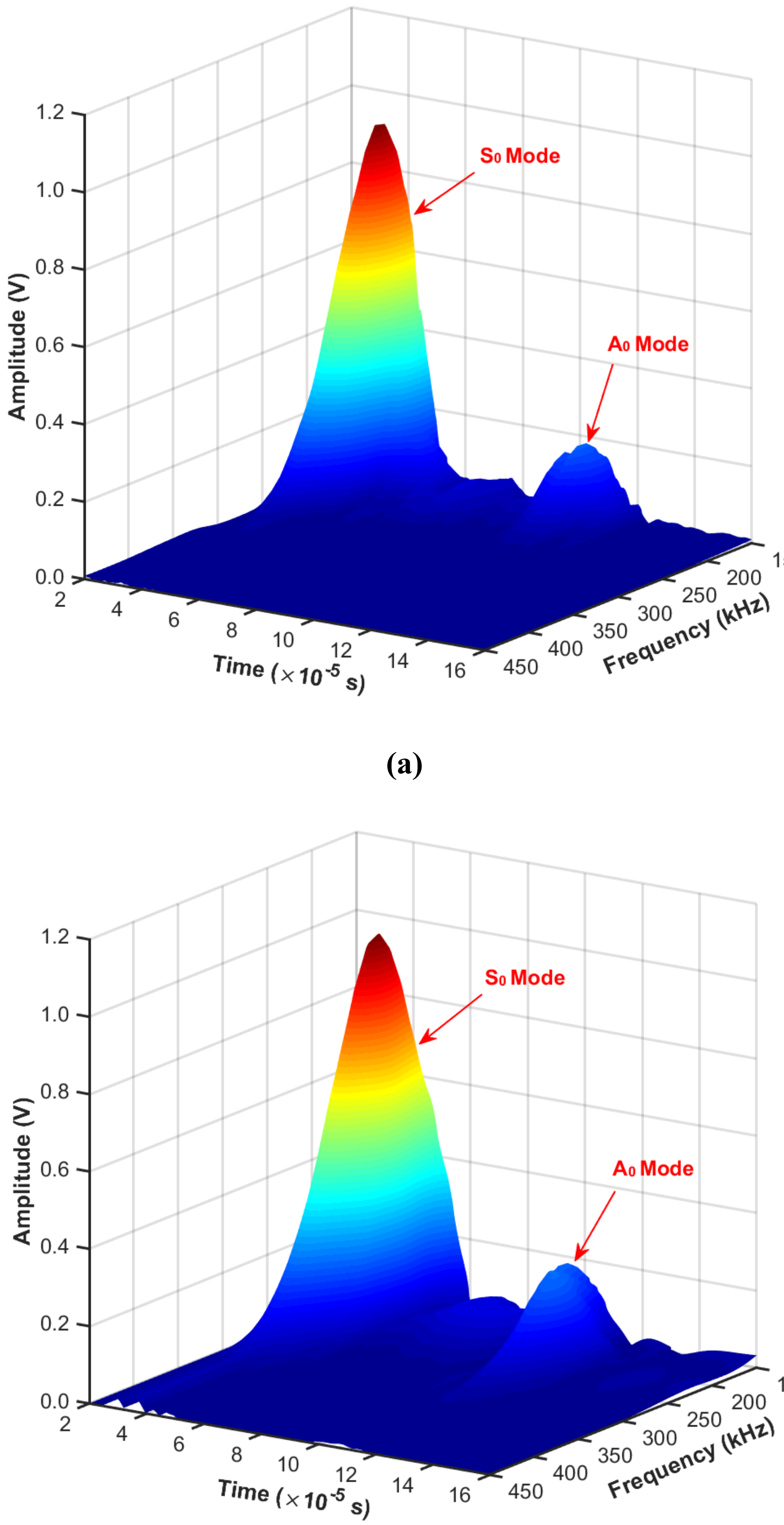

(a)

(b)

Fig. 11. Spectra of signals under sweep frequency excitation for (a) the implanted sensing unit; (b) the embedded PZT wafer (captured along sensing path P1 – S5).

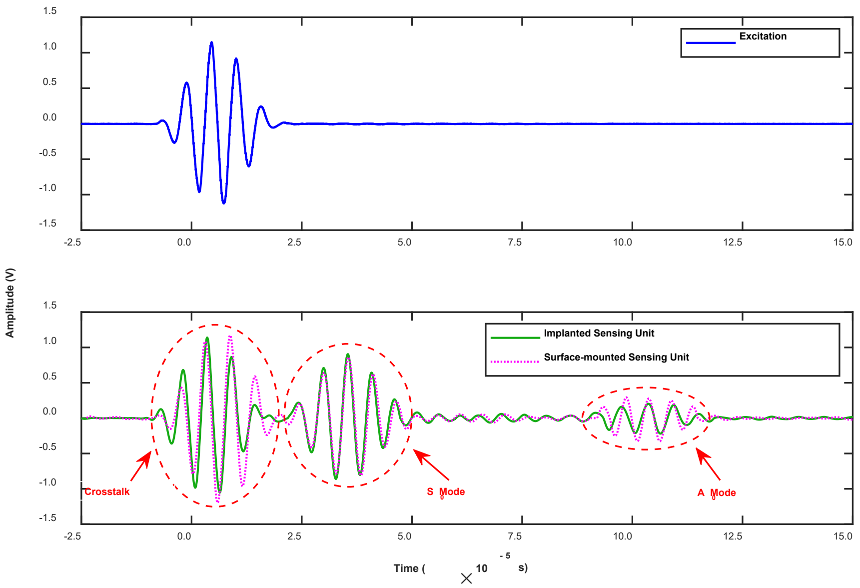

Fig. 12. GUWs signals respectively captured by the implanted and surface-mounted sensing units along sensing path P1 – S5 at 175 kHz.

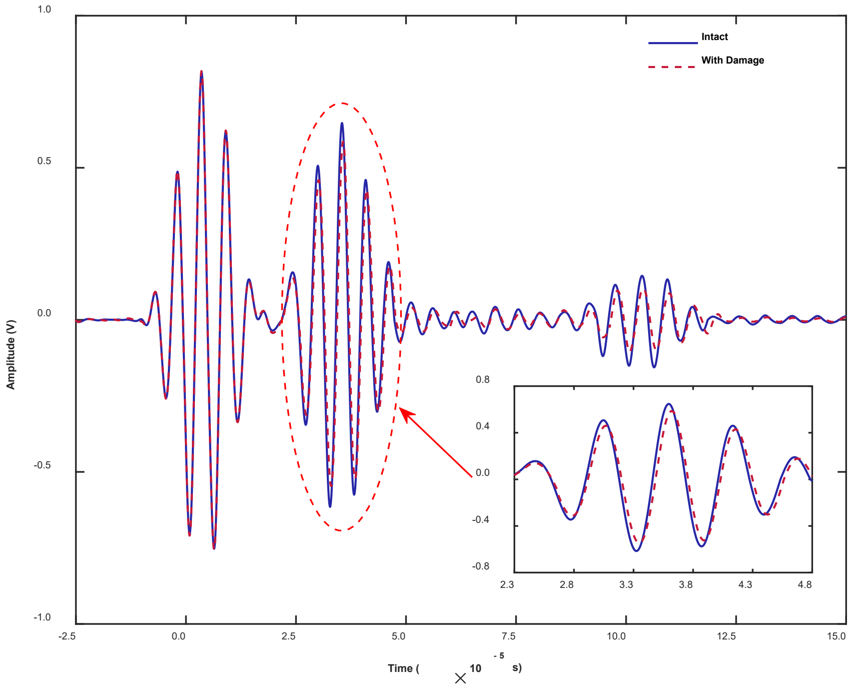

Fig. 13. Signals captured by the implanted sensing unit along sensing path P1 – S5 at 175 kHz, before and after artificial anomaly introduced.

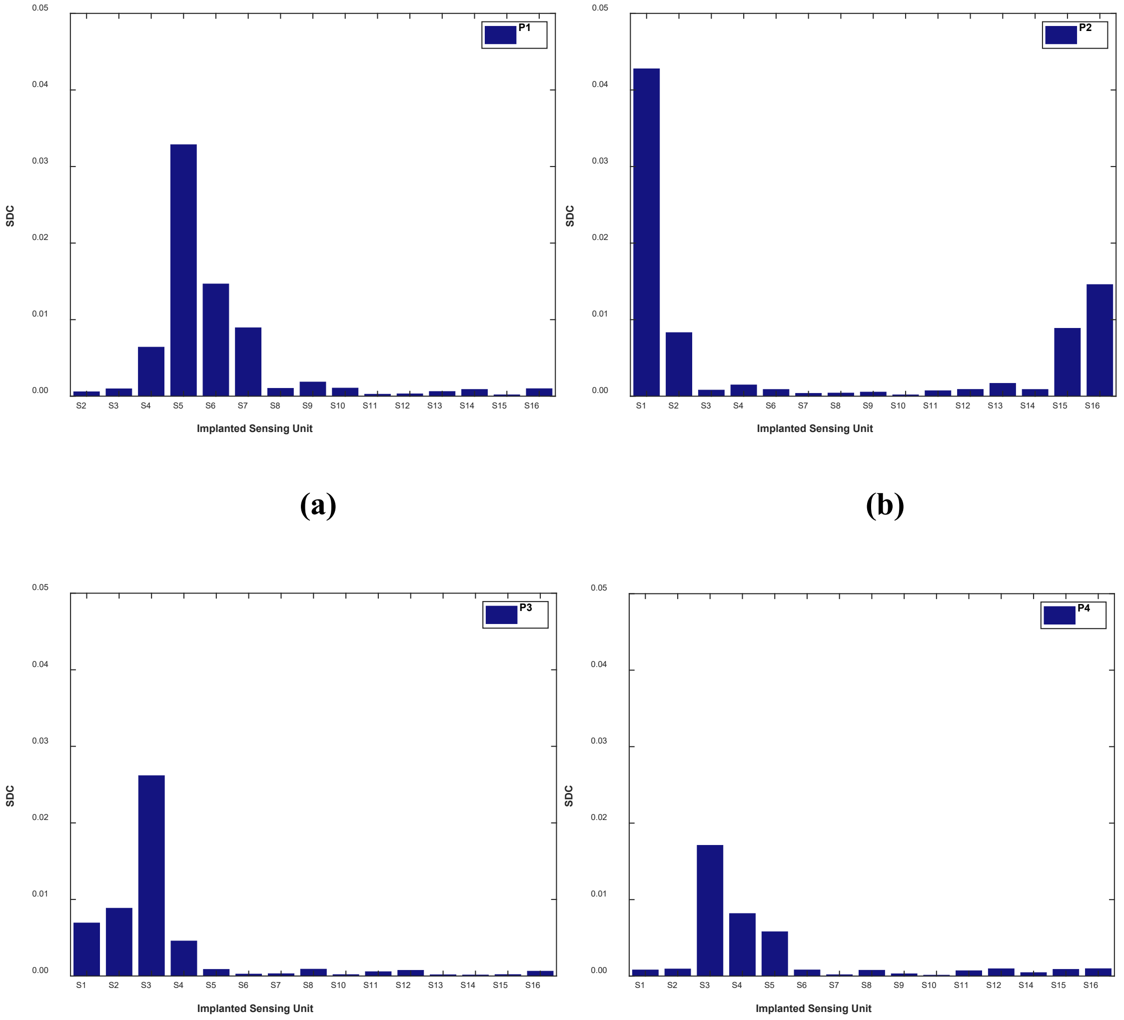

(a) **(b)**

(c) **(d)**

Fig. 14. Calculated SDC values for different sensing paths when (a) P1, (b) P2, (c) P3, and (d) P4 are used as the wave actuator.

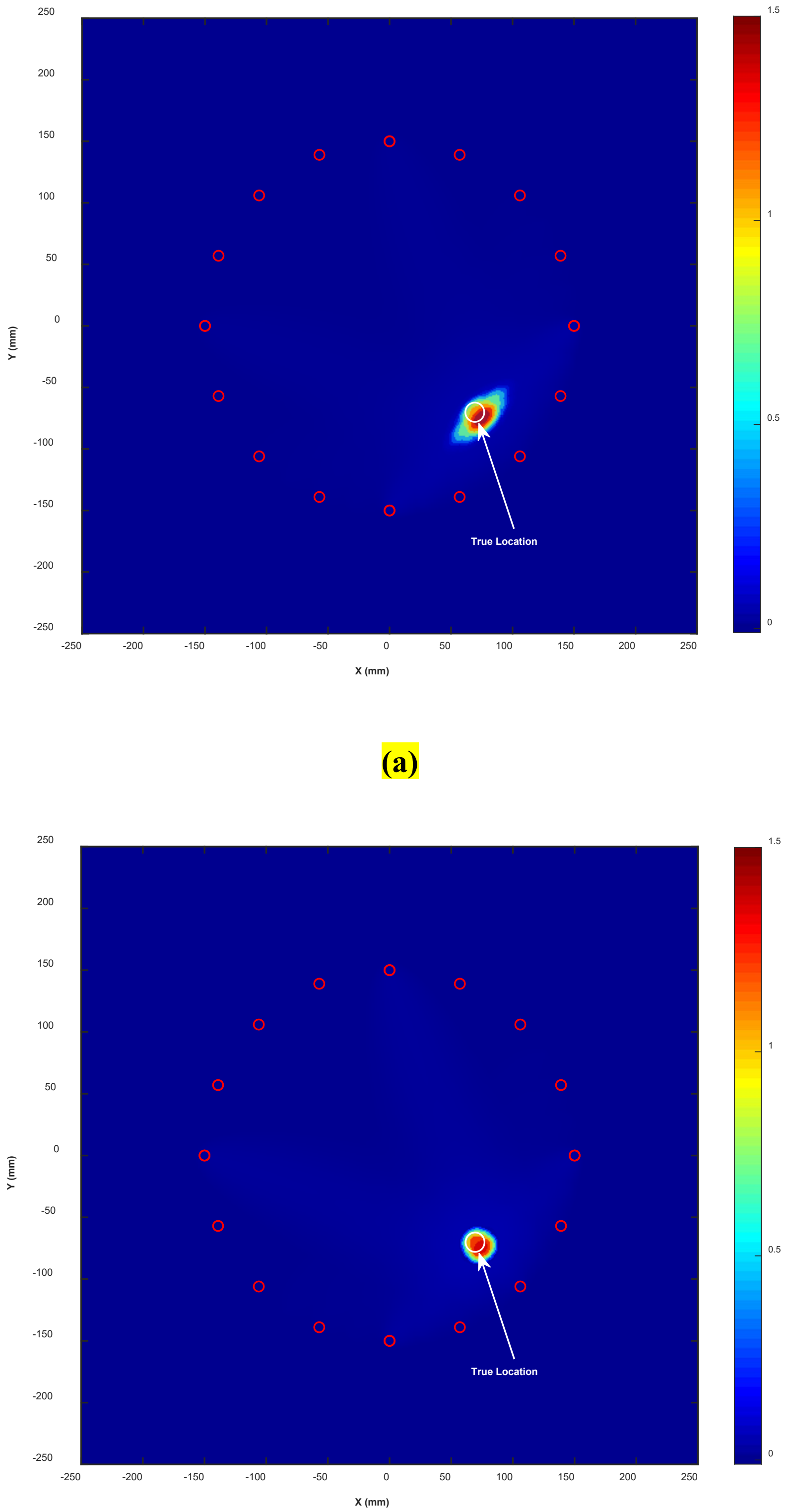

(a)

(b)

Fig. 15. Tomographic images constructed using (a) conventional, and (b) enhanced RAPID algorithms.